Covalent organic framework photocatalysts for green and efficient photochemical transformations

Yongzhi Chen [1], Yuanyuan Guo[2], Tie Wang [3], Sailun Ji[4], Haipei Shao[1,5], Ming Lin [5], Shu Seki [4], Ning Yan [3] & Donglin Jiang [1] ✉

Artificial photosynthesis is impeded by rapid charge recombination and inefficient use of photogenerated carriers. Here we present covalent organic frameworks with systematically tailored skeletons and pores for green yet efficient photosynthesis with water and air. The hexavalent frameworks with non-conjugated photocatalytic skeletons enable water oxidation at knot corners and oxygen reduction at linker edges, while orientated triangular micropores timely supply water and air. Noteworthily, the framework with the highest π density and smallest supermicropores exhibits optimal charge separation and utilization and achieves rapid, efficient and cyclable hydrogen peroxide production in both batch and membrane reactors. Remarkably, the supermicroporous framework instantly removes organic dye contaminants from water and fully degrades these dyes under visible light. Our findings enable a paradigm shift to the systematic design of both electron/hole flow and mass transport for constructing photocatalysts, which are not only scientifically important but also technologically key to shaping sustainable society and future.

Water is the source of all life and the most important liquid in ecosystem[1–4]. Notably, it participates in the fundamental process of photosynthesis, through which plants transform carbon dioxide and water into sugars and oxygen (Fig. 1a). This process is indispensable, providing the primary input of free energy into the biosphere and establishing the foundation for evolution. Inspired by natural photosynthesis, artificial photosynthesis has been targeted to capture and store sunlight energy in the chemical bonds of solar fuels[5–10]. Despite advances over the past half-century, artificial photosynthesis remains challenging due to quick dissipation of excitation energy as heat and low efficiency use of photogenerated electrons and holes[11–15].

Since the first oil shock crisis in 1970s, tremendous efforts have been dedicated to the studies on photocatalysts. Over that past five decades, although various photocatalytic materials have been investigated[16–18], however, most systems rely on the use of sacrificial agents and suffer from low efficiency[19–23]. Typical semiconductors such as TiO_2 suffer from wide bandgaps, limited absorption ranges and low efficiency. Resorcinol–formaldehyde resins are cost effective, but they have extremely low surface area and limited structural tunability. Graphitic carbon nitride (g-C_3N_4), a representative organic photocatalyst, struggles with narrow absorption range, rapid charge recombination and poor dispersibility. Metal–organic frameworks (MOFs) are tunable in structures, but they face moisture sensitivity and metal leaching risks. It is highly desirable to develop innovative photocatalysts with tailor-made robust structures and outstanding photocatalytic performance.

[1]Department of Chemistry, Faculty of Science, National University of Singapore, 3 Science Drive 3, Singapore 117543, Singapore. [2]School of Science, Beijing University of Posts and Telecommunications, Beijing 100876, China. [3]Department of Chemical and Biomolecular Engineering, National University of Singapore, 4 Engineering Drive 4, Singapore 117585, Singapore. [4]Department of Molecular Engineering, Graduate School of Engineering, Kyoto University, Katsura, Nishikyo-ku, Kyoto 615-8510, Japan. [5]Institute of Materials Research and Engineering, Agency for Science (IMRE), Technology and Research (A*STAR), 2 Fusionopolis Way, Innovis #08-03, Singapore 138634, Singapore. ✉e-mail: chmjd@nus.edu.sg
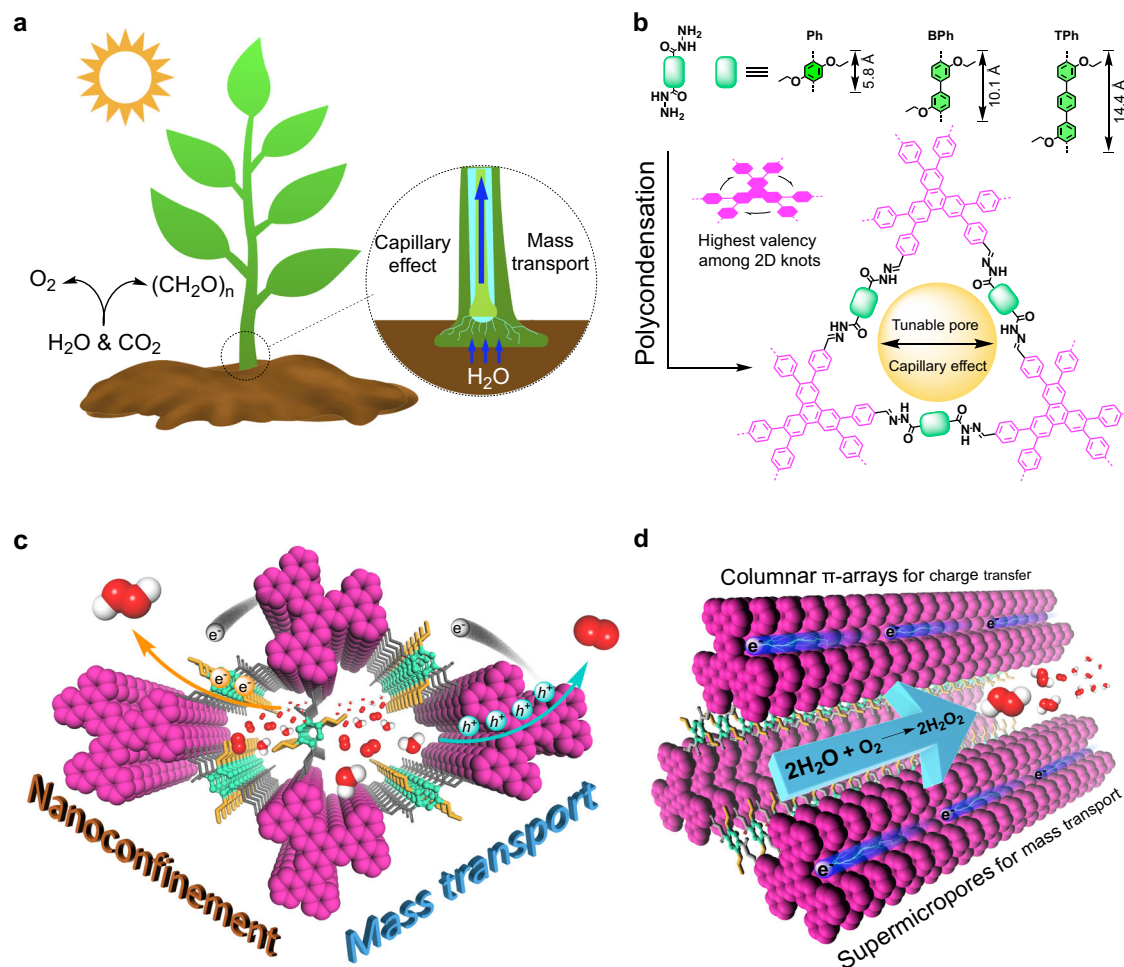
Fig. 1 | Natural and artificial photosynthesis. a Plants convert H_2O and CO_2 into O_2 and carbohydrates via natural photosynthesis. Inset: Capillary effect for water transport. **b** Hexavalent COFs with precisely tuned skeletons and trigonal supermicropores for artificial photosynthesis. **c** Schematic of hexavalent supermicroporous COFs for artificial photosynthesis through water oxidation at knot and oxygen reduction at linker. **d** Schematics of charge transport/accumulation in π columns and water/oxygen delivery through 1D channels, enabling photosynthesis of H_2O_2 with water and oxygen.

For artificial photosynthesis, two distinct systems are essential: one for the production, transport and utilization of photogenerated electrons and holes[24–27], which relies on π skeletons, and another for the supply, confinement and activation of water and oxygen[28–33], which depends on pore structures. Covalent organic frameworks (COFs) stand out in this context, as they offer ordered π skeletons and inherent pores with high structural tunability[34–36], making them ideal platforms for artificial photosynthesis[11–13]. Although COFs with different structures have been studied, rational design for efficient photosynthesis remains challenging, while the roles of their skeletons and pores are still unclear.

Hydrogen peroxide (H_2O_2) is one of the most important compounds with versatile use as an environmentally benign oxidant for medical and chemical industries, and as a convenient liquid energy carrier for fuel cells[16,37]. Industrial mainstream protocol for H_2O_2 production is anthraquinone method[38–41], which is highly energy demanding, employs high-pressure hydrogen and toxic organic solvents and uses expensive noble metals as catalysts. Furthermore, this technology accompanies with intense post purification processes and generates substantial chemical wastes. Hence, it is highly desired to develop energy-efficient, mild, green and sustainable routes for H_2O_2 production.

In this study, we design photocatalytic COFs with precisely tuned π skeletons and pores to elucidate their critical roles in charge utilization and water/oxygen activation, leading to the discovery of efficient photosynthesis to produce H_2O_2 efficiently using water and air (Fig. 1b–d). Our study reveals key insights into the photosynthetic process: (1) With hexavalent connectivity, which offer the highest density of π units among all topologies (Fig. 1b), the resultant COFs maximize light-harvesting activity, charge transport and accumulation and catalytic centre density. (2) The spatial separation of water oxidation and oxygen reduction centres− confining them at acute knot corners and open linker edges, respectively−enhances charge separation and prevents charge recombination (Fig. 1c). (3) Nanogrooves offer acute space to confine and activate water and oxygen molecules, facilitating both water oxidation and oxygen reduction (Fig. 1c). (4) One-dimensional (1D) trigonal supermicropores with aligned single-file oxygen chains on the pore walls trigger strong capillary effects, delivering water and oxygen timely to the catalytic centres (Fig. 1d). Remarkably, the supermicropore COFs enable instant removal of organic dye contaminants from water and fully and rapidly degrade them under visible light. Our photocatalysts feature green yet efficient photo-to-chemical transformations in both batch and membrane reactors under ambient conditions, only requiring water, air and light as inputs.

Results

Design principle and synthesis
We designed two-dimensional (2D) trigonal COFs featuring hexavalent superlattices and supermicroporous structures, which offer the

highest density of π units and the smallest pores among all 2D COF topologies (Fig. 1 and Supplementary Fig. 1). The non-conjugated yet dense knot and linker π arrays act as light-harvesting antennae, which, upon photoirradiation, transform into catalytic centres for water oxidation and oxygen reduction (Fig. 1c). The supermicroporous structures, with their trigonal topology, form three notched nanogrooves with acute angles of 60° (Fig. 1d). These trigonal pores create an exceptionally confined and greatly constraint environment for water and oxygen molecules.

Three hydrazone-linked COFs (Supplementary Fig. 2), namely HPTP-Ph-COF, HPTP-BPh-COF and HPTP-TPh-COF were synthesized by condensing 2,3,6,7,10,11-hexakis(4-formylphenyl) triphenylene (HPTP) as knot with 2,5-diethoxyterephthalohydrazide (Ph), 3,3′-diethoxy-(1,1′-biphenyl)−4,4′-dicarbohydrazide (BPh) and 3,3″-diethoxy-(1,1′:4′,1″-terphenyl)−4,4″-dicarbohydrazide (TPh) as linkers at 150 °C in 91%, 87% and 88% yields, respectively (see synthetic procedures in Methods and Supplementary Information Section 2.2). In these COFs, each HPTP knot is linked with six linker units, while each linker bridges two knots, forming extended 2D hexavalent π skeletons and orientated 1D triangular pores (Supplementary Fig. 2b–g).

Structural characterization

The hydrazone-linked COFs were ambiguously characterized with various methods. HPTP-Ph-COF (Supplementary Fig. 3), HPTP-BPh-COF (Supplementary Fig. 4) and HPTP-TPh-COF (Supplementary Fig. 5) exhibited C=O stretch at 1671–1668 cm^{-1}, C=N stretch at 1610–1604 cm^{-1} and N–H stretch at 3288–3282 cm^{-1}. Solid state ^{13}C cross polarization magic angle spinning nuclear magnetic resonance spectroscopy (SS ^{13}C CP/MAS NMR) verified their backbone structures as well as the distinct carbon signal of the ethoxy chains in HPTP-Ph-COF (Supplementary Fig. 6), HPTP-BPh-COF (Supplementary Fig. 7) and HPTP-TPh-COF (Supplementary Fig. 8). These COFs show rod-like morphology (Supplementary Fig. 9) and have a thermal stability over 240 °C under N_2 (Supplementary Fig. 10). High resolution transmission electron microscopy (HR TEM) revealed highly ordered and porous structures of COFs (Supplementary Fig. 11), which agree with the results of PXRD and reconstructed structures. The derived FFT images revealed clear diffraction points that originate from the (100) facets (insets of Supplementary Fig. 11). X-ray photoelectron spectroscopy (XPS) disclosed signals of C, N and O elements from the COF skeletons (Supplementary Fig. 12). Specifically, the C $1s$ region (Supplementary Fig. 12a) identified characteristic peaks of C–C and C–O at 284.7 and 286.1 eV, respectively. The N $1s$ region (Supplementary Fig. 12b) identified characteristic signal of C=N bond at 399.8 eV, and the O $1s$ region (Supplementary Fig. 12c) identified characteristic peaks of C=O and C–O bonds at 531.8 and 533.7 eV, respectively.

HPTP-Ph-COF (Fig. 2a, blue cross) exhibited powder X-ray diffraction (PXRD) peaks at 3.40°, 6.00°, 6.87°, 9.15°, 10.48° and 25.39°, which were assigned to the (100), (110), (200), (210), (300) and (001) facets, respectively. As a result of the elongation of linker from phenyl to biphenyl and terphenyl, the peak positions left-shifted to 3.03°, 5.31°, 6.04°, 8.08°, 9.16°, 15.25°, 25.16° for HPTP-BPh-COF (Fig. 2b, blue cross) and 2.75°, 4.72°, 5.44°, 8.15°, 24.82° for HPTP-TPh-COF (Fig. 2c, blue cross), respectively. Notably, these peak intensities and positions agree well with their simulated PXRD patterns of AA stacking modes (Fig. 2a–c, green curves). Pawley refinement (for atomistic coordinates, see cif files) revealed negligible differences (Fig. 2a–c, grey curves) from the experimental results, showing small R_{wp} and R_p values of 6.10% and 4.62% for HPTP-Ph-COF, 4.02% and 2.82% for HPTP-BPh-COF, and 4.61% and 2.48% for HPTP-TPh-COF, respectively. HPTP-Ph-COF (Fig. 2d, g), HPTP-BPh-COF (Fig. 2e, h) and HPTP-TPh-COF (Fig. 2f, i) develop trigonal topology with unit cell parameters of $a = b = 3.00$ nm, $c = 3.51$ Å, $\alpha = 90.0°$, $\beta = 90.0°$ and $\gamma = 61.6°$, $a = b = 3.46$ nm, $c = 3.55$ Å, $\alpha = 90.3°$, $\beta = 90.5°$ and $\gamma = 61.1°$, and $a = b = 3.89$ nm, $c = 3.67$ Å, $\alpha = 89.9° \beta = 90.1°$ and $\gamma = 59.5°$, respectively.

Hexavalent skeletons for charge separation, transport and accumulation

HPTP-Ph-COF (Fig. 3a, green curve), HPTP-BPh-COF (orange curve) and HPTP-TPh-COF (blue curve) exhibited an absorption edge at 453, 448 and 442 nm, respectively. HPTP-Ph-COF (Fig. 3b, green curve), HPTP-BPh-COF (orange curve) and HPTP-TPh-COF (blue curve) showed an optical energy bandgap of 2.82, 2.85 and 2.87 V, respectively. Their conduction band (CB) (vs. NHE, pH = 6.8) locates at −1.27, −1.20 and −1.23 V (Supplementary Figs. 13–15), respectively, while their valence band (VB) positions at 1.55, 1.65 and 1.64 V, respectively (Fig. 3c). All COFs exhibited high enough VB levels to enable water oxidation reaction (Fig. 3c, dashed red line, +0.83 V) and suitable CB levels for oxygen reduction reaction (Fig. 3c, dashed magenta line, −0.35 V).

Owing to the non-conjugated hydrazone linkage between knot and linker, HPTP-Ph-COF (Supplementary Fig. 16a, d), HPTP-BPh-COF (Supplementary Fig. 16b, e) and HPTP-TPh-COF (Supplementary Fig. 16c, f) localized the highest occupied molecular orbital (HOMO) on hexaphenyl triphenylene knots and the lowest unoccupied molecular orbitals (LUMO) on phenyl-based linkers. We highlight that this electronically segregated HOMO at knot and LUMO at linker is critical for photosynthesis owing to its three-fold functions: (1) It prevents charge recombination and facilitates charge separation. (2) It promotes both hole and electron transport along the z-axis and enables charge accumulation in the stacked knot and linker π-arrays. (3) It converts knot and linker arrays to water oxidation and oxygen reduction centres, respectively, once the frameworks are shed with light to trigger charge separation.

The projected density of states (PDOS) revealed that the electron population in the p-orbital near its VB edge is much denser in HPTP-Ph-COF (Fig. 3d) than those in HPTP-BPh-COF (Supplementary Fig. 17) and HPTP-TPh-COF (Supplementary Fig. 18), suggesting that HPTP-Ph-COF is much easier to be photoexcited. Exciton dynamics revealed that HPTP-Ph-COF (Fig. 3e, green curve, 0.69 ns) allows faster charge separation than HPTP-BPh-COF (orange curve, 1.00 ns) and HPTP-TPh-COF (blue curve, 1.16 ns) as evident by a shorter fluorescence lifetime. To reveal photoexcited state dynamics, we performed transient absorption spectroscopy (TA). The formation of a negative feature in TA spectra within 1 ps (Supplementary Figs. 19–21) can be attributed to the combined ground state bleaching and stimulated emission, while a broad positive feature that extends to the infrared region can be assigned to photoinduced absorption. Additionally, comparative studies on kinetics of these three COFs revealed that HPTP-Ph-COF (Fig. 3f, green circle) develops a long-lived charge separation state with a lifetime of 578.3 ps, while HPTP-BPh-COF (orange circle) and HPTP-TPh-COF(blue circle) exhibited shorter charge separation state with lifetimes of 443.1 and 236.2 ps (Supplementary Table 1), respectively. The longer lifetime for HPTP-Ph-COF enables the efficient utilization of photoinduced charges, endowing the system with a superior photocatalytic performance.

Impedance and photocurrent experiments revealed that HPTP-Ph-COF has the smallest charge transport resistance (Fig. 3g, green circle) and the largest photocurrent (Fig. 3h, green curve) in comparison to HPTP-BPh-COF (Fig. 3g, orange circle; Fig. 3h, orange curve) and HPTP-TPh-COF (Fig. 3g, blue circle; Fig. 3f, blue curve). Flash-photolysis time-resolved microwave conductivity (FP-TRMC) measurements as a contactless and electrode-free technique are useful to characterize inherent charge carrier mobility (Fig. 3i and Supplementary Fig. 22), which revealed that HPTP-Ph-COF (Supplementary Fig. 22, green curve), HPTP-BPh-COF (orange circle) and HPTP-TPh-COF (blue circle) have a comparable transient photoconductivity of about 1.0×10^{-9} m^2 V^{-1} s^{-1} (Supplementary Table 2). Upon chemical oxidation with nitrobenzene, HPTP-Ph-COF (Fig. 3i, green curve) increased the transient photoconductivity to 2.0×10^{-9} m^2 V^{-1} s^{-1} with a 122.2% increment, while HPTP-BPh-COF (orange curve) increased by 110% and HPTP-TPh-COF (blue curve) decreased by 72.7% (Supplementary Table 2).
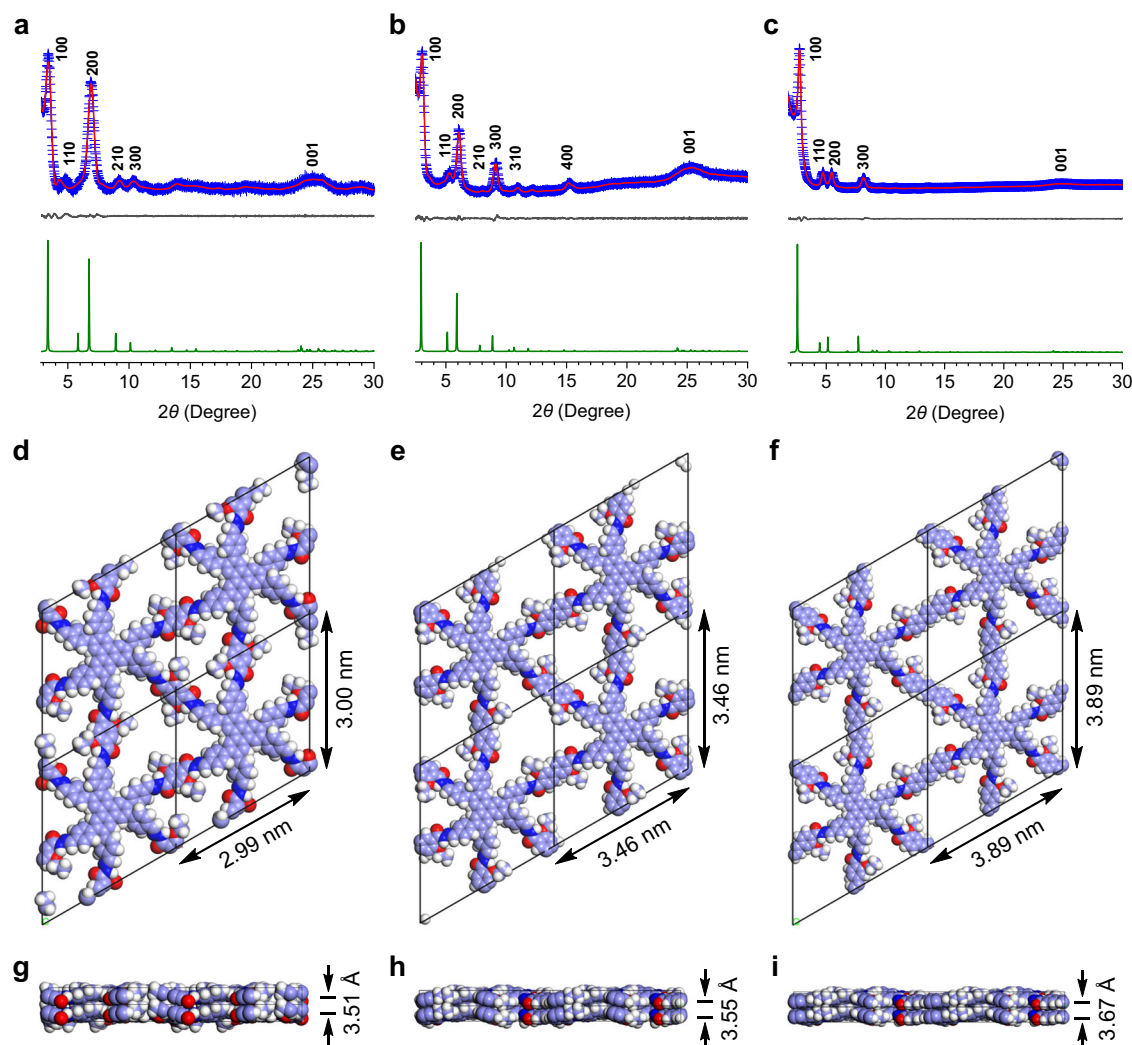
Fig. 2 | Crystal structures. a–c Experimentally obtained PXRD patterns (blue cross), Pawley refined patterns (red curves), their differences (grey curves) and AA-stacking patterns (green curves) of HPTP-Ph-COF (**a**), HPTP-BPh-COF (**b**) and HPTP-TPh-COF (**c**). **d–f** The top views of unit cells of HPTP-Ph-COF (**d**), HPTP-BPh-COF (**e**) and HPTP-TPh-COF (**f**). **g–i** The side views of unit cells of HPTP-Ph-COF (**g**), HPTP-BPh-COF (**h**) and HPTP-TPh-COF (**i**).

Through these experimental and computational studies, we revealed key parameters for the rational design of skeletons: (1) The hexavalent connectivity allows the integration of π units into the lattice with the highest density among all 2D COFs. (2) The non-conjugated hydrazone linkage is essential to electronically separate the HOMO and LUMO levels, which make not only charge separation and accumulation but also conversion of knot and linker arrays into oxidation and reduction centres possible. This is the first must for designing COFs to drive photosynthesis without the need for sacrificial agents and co-catalysts. (3) Minimizing the trigonal lattice exerts profound impacts on charge separation, transport and accumulation. The skeleton with the shortest phenyl edge concentrates electron density, reduces charge recombination, enlengthens charge separation state, decreases resistance, and facilitates charge transport and accumulation. This elaborate molecular management with precision leads to these findings and uncovers the hidden roles of skeletons for photosynthesis.

Supermicropores for water/oxygen transport, confinement and activation

HPTP-Ph-COF (Supplementary Fig. 23), HPTP-BPh-COF (Supplementary Fig. 24) and HPTP-TPh-COF (Supplementary Fig. 25) exhibited Brunauer-Emmett-Teller (BET) surface areas of 742, 844 and 624 $m^2 g^{-1}$,

pore sizes of 0.97/1.40 nm, 1.30/1.60 nm and 1.42/1.89 nm, and pore volumes of 0.27, 0.34 and 0.23 $cm^3 g^{-1}$ (Supplementary Table 3), respectively, as revealed by nitrogen sorption isotherm measurements. This result confirmed that minimizing the trigon edge length is accompanied with a precise tune of triangular pore size from 1.9 nm to 1.4 nm and 0.97 nm. HPTP-Ph-COF has the smallest pores in trigonal COFs.

Water vapor sorption experiments (Supplementary Fig. 26 and Supplementary Table 4) revealed that HPTP-Ph-COF has the smallest induction P/P_0 zone of 0–0.15 and sharpest capillary effect within a P/P_0 zone of 0.15–0.22 at 298.15 K. In contrast, HPTP-BPh-COF and HPTP-TPh-COF exhibited more broad induction P/P_0 zones of 0–0.23 and 0–0.35 and sluggish capillary P/P_0 zones of 0.23–0.35, 0.35–0.50, respectively. This trend is also observed for temperatures at 283.15 K (Supplementary Fig. 27) and 288.15 K (Supplementary Fig. 28). Notably, HPTP-Ph-COF, HPTP-BPh-COF and HPTP-TPh-COF exhibited water adsorption capacities of 0.261, 0.279 and 0.177 $g g^{-1}$ at $P/P_0 = 0.9$ and 298.15 K (Supplementary Table 4), and heat of adsorption (Q_{st}) of 47.6, 46.8 and 46.9 $kJ mol^{-1}$ (Supplementary Figs. 29–31), respectively. HPTP-Ph-COF (Supplementary Fig. 32, green bar) exhibited the highest pore occupancy of 96.9% at 298.15 K, while HPTP-BPh-COF (orange bar) and HPTP-TPh-COF (blue bar) displayed a decreased pore occupancy of 82.4% and 77.3%, respectively. These results revealed that
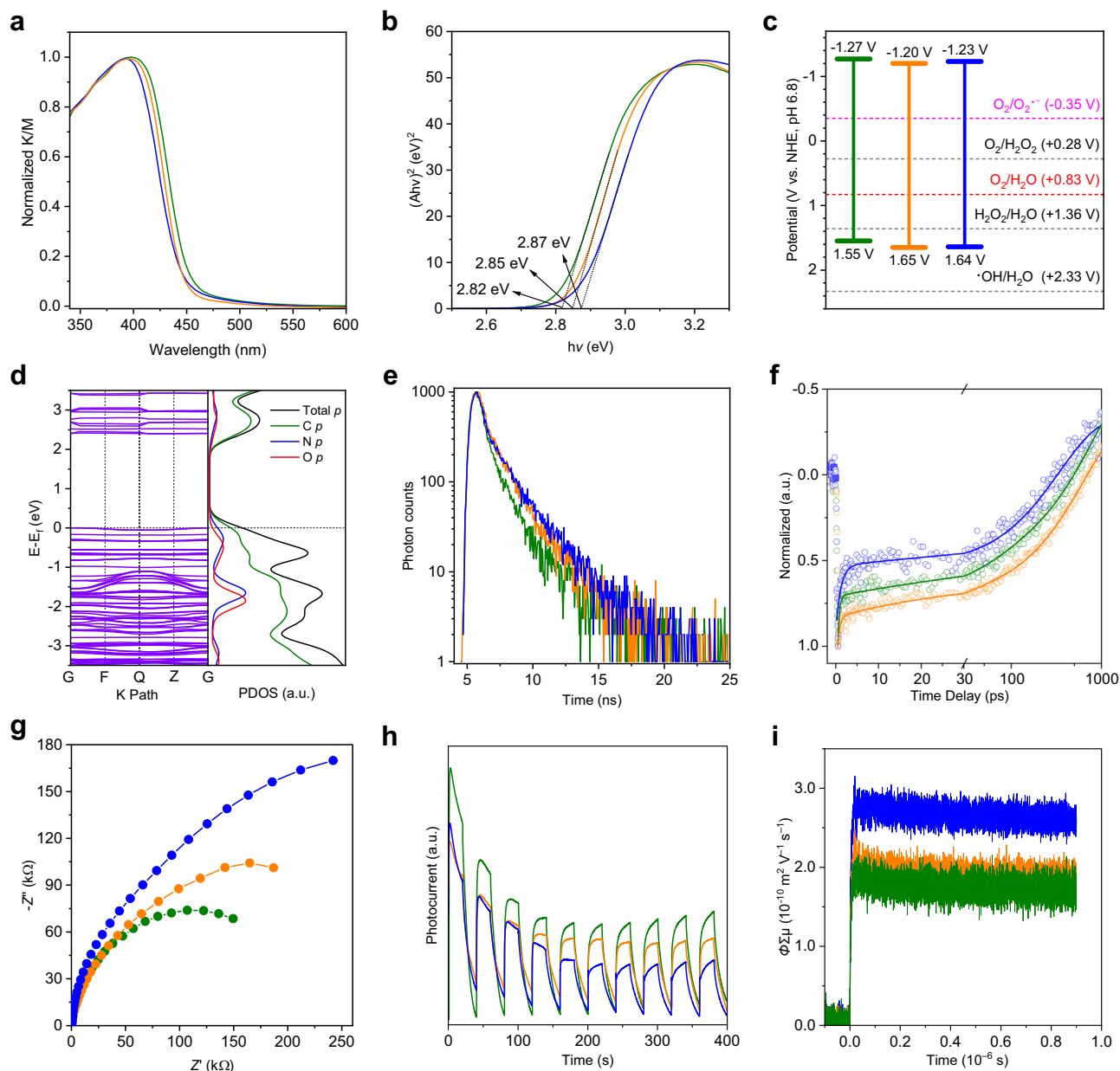
Fig. 3 | Photophysical and photoconductivity properties. a Solid-state electronic absorption spectra. **b** Tauc plots. **c** Experimentally derived energy band alignment (vs NHE at pH 6.8) compared to potentials for oxygen reduction (dotted pink line at −0.35 V) and oxygen evolution (dotted red line at +0.83 V), along with other possible reactions. **d** Band structure and projected density of states (PDOS) of HPTP-Ph-COF. **e** Fluorescence decay profiles. **f** Transient absorption kinetic traces at 700 nm. **g** Electrochemical impedance spectra. **h** Photocurrent generation. **i** Kinetic traces of flash-photolysis time-resolved microwave conductivity (FP-TRMC) transients observed for the nitrobenzene-doped COFs. In (**a**–**c**) and (**e**–**i**), green, HPTP-Ph-COF; orange, HPTP-BPh-COF; blue, HPTP-TPh-COF.

HPTP-Ph-COF enables stronger water confinement than HPTP-BPh-COF and HPTP-TPh-COF.

Electrostatic potential calculations revealed that HPTP-Ph-COF (Supplementary Fig. 33a) develops a more polarized pore wall, compared to HPTP-BPh-COF (Supplementary Fig. 33b) and HPTP-TPh-COF (Supplementary Fig. 33c), confirming its improved hydrophilicity for water confinement. Indeed, HPTP-Ph-COF (Supplementary Fig. 34a) is hydrophilic to display a contact angle of 79.4°, while HPTP-BPh-COF (Supplementary Fig. 34b) and HPTP-TPh-COF (Supplementary Fig. 34c) have a much larger water contact angle of 93.6° and 97.1°, respectively. The water confinement was further revealed by differential scanning calorimetry (DSC) measurements. Noticeably, the freezing points of water clusters decreased significantly to −38.04 °C in HPTP-Ph-COF (Supplementary Fig. 35a), −38.67 °C in HPTP-BPh-COF (Supplementary Fig. 35b) and −36.05 °C in HPTP-TPh-COF (Supplementary Fig. 35c), respectively, indicating strong nanoconfinement effects in these supermicropore COFs.

The different water behaviours originate from different pore wall structures. HPTP-Ph-COF (Supplementary Fig. 35d) possesses a high percentage of heteroatoms, i.e., oxygen and nitrogen, in comparison to HPTP-BPh-COF (Supplementary Fig. 35e) and HPTP-TPh-COF (Supplementary Fig. 35f). As the pore walls of these COFs are covered with carpets of dense C–H units protruded from the knot and linker, these heteroatom oxygen and nitrogen chains on pore walls provide interactive sites for confining water and dissolved oxygen molecules. These interactions are greatly reinforced as the pore size is reduced, triggering the highest hydraulic sensitivity for the smallest supermicropores.
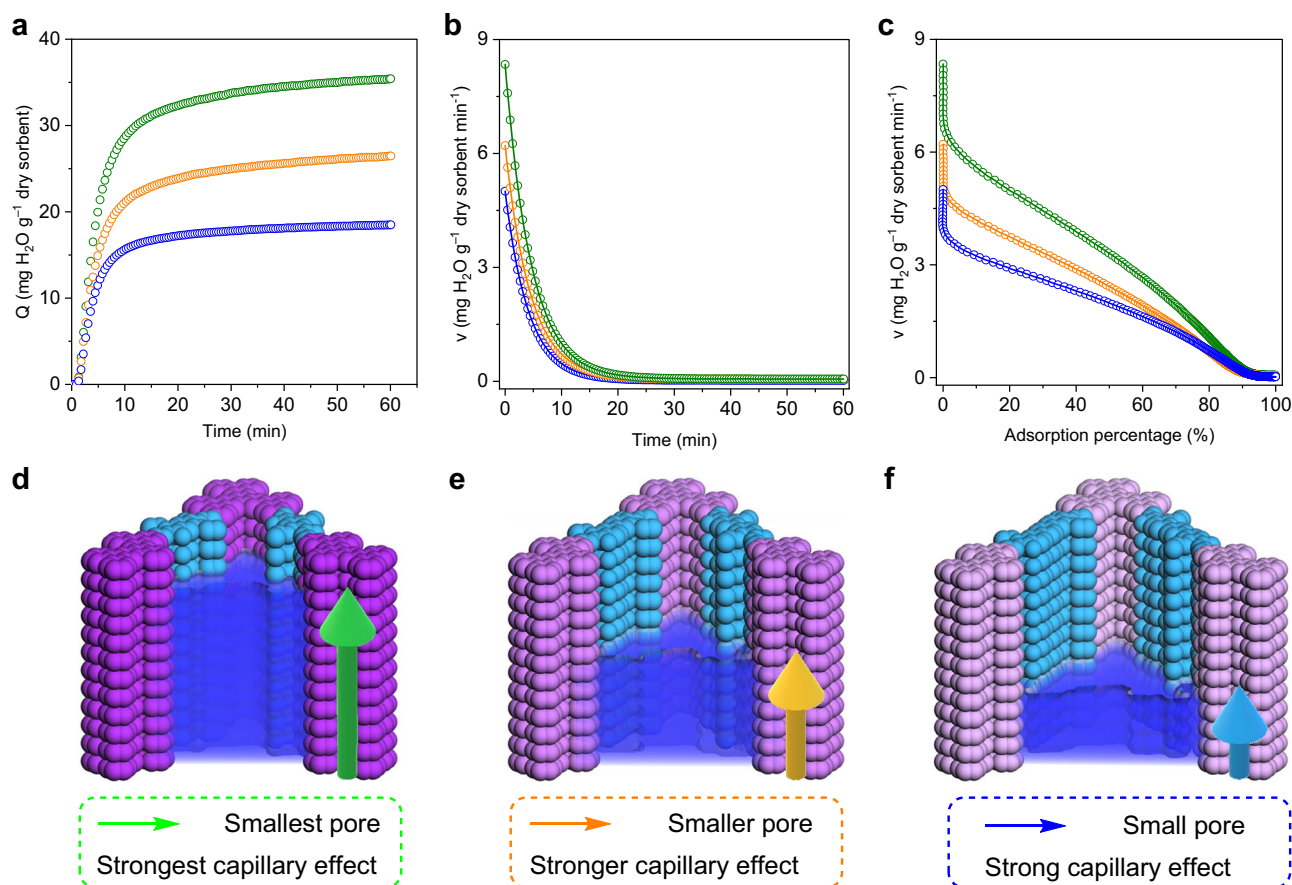
Fig. 4 | Water transport and capillary effect. a Dynamic water adsorption profiles. **b** Transfer rate−time variation curves. **c** Transfer rate−adsorption percentage variation curves. **d**−**f** Pore size-dependent capillary effect in HPTP-Ph-COF (**d**), HPTP-BPh-COF (**e**) and HPTP-TPh-COF (**f**). In (**a**−**c**), green, HPTP-Ph-COF; orange, HPTP-BPh-COF; blue, HPTP-TPh-COF.

Dynamic vapor sorption measurements revealed that HPTP-Ph-COF (Fig. 4a, green circle), HPTP-BPh-COF (orange circle) and HPTP-TPh-COF (blue circle) are distinct in water adsorption kinetics (Supplementary Figs. 36−38 and Supplementary Table 5). The plot of water flow rate as a function of time (Fig. 4b) revealed that HPTP-Ph-COF (green curve) achieves the highest water flow rate of 8.34 mg H_2O g^{-1} COF min^{-1}, which is 6.21 and 5.01 mg H_2O g^{-1} COF min^{-1} for HPTP-BPh-COF (orange curve) and HPTP-TPh-COF (blue curve), respectively. Notably, the plot of water flow rate as a function of adsorption percentage (Fig. 4c) verified that at any time stage, HPTP-Ph-COF (green curve) enables a higher water flow rate than HPTP-BPh-COF (orange curve) and HPTP-TPh-COF (blue curve).

Through molecular design of trigonal micropores with discrete pore size and pore wall surface structures, we revealed key parameters for the rational design of pores: (1) The trigonal pores develop constraint acute walls that facilitate capillary effect, compared to all other topologies of 2D COFs[2,12]. (2) The smallest trigonal supermicropores trigger the strongest capillary effect, and enable low-energy, rapid and full water uptake. (3) The smallest supermicropores allow water super flow across the 1D channels to reach a rate as high as 4.5×10^{18} H_2O molecules s^{-1} (Fig. 4d−f, per gram COF). The combination of strong confinement and rapid delivery of reactants favourites the effective use of charges for photosynthesis[28,32,33].

Photosynthesis in batch reactors
HPTP-Ph-COF (3.0 mg) enables a rapid photocatalytic reaction of aerated water (15 mL) under visible light irradiation ($\lambda = 420−600$ nm)

and ambient conditions (see photocatalytic procedures in Supplementary Information Section 1.23 and Supplementary Fig. 39), attaining a H_2O_2 concentration as high as 1.73 mM within 60 min (Fig. 5a, green curve). Under otherwise identical conditions, HPTP-BPh-COF (orange curve) and HPTP-TPh-COF (blue curve) yielded a H_2O_2 concentration of only 1.27 and 0.82 mM, respectively. Accordingly, the H_2O_2 production rate is 8.6 mmol g^{-1} h^{-1} for HPTP-Ph-COF (Fig. 5b, green bar), 6.4 mmol g^{-1} h^{-1} for HPTP-BPh-COF (orange bar) and 4.1 mmol g^{-1} h^{-1} for HPTP-TPh-COF (blue bar). The amorphous HPTP-Ph polymer with the same composition as HPTP-Ph-COF, exhibited a much lower H_2O_2 production rate of 2.0 mmol g^{-1} h^{-1} (Supplementary Fig. 40), demonstrating the importance of ordered structure for photosynthesis. A stoichiometric mixture (3/1 in mole) of knot (1.6 mg) and linker (1.6 mg) presented a H_2O_2 generation rate of only 0.3 mmol g^{-1} h^{-1} (Supplementary Fig. 40), indicating the vital role of crystalline porous frameworks.

We conducted a series of control experiments with hexagonal non-conjugated TFPB-Ph-COF (Supplementary Figs. 41−43 and Supplementary Note 1), trigonal partially π-conjugated Im-HPTP-Ph-COF (Supplementary Figs. 44−46) and fully π-conjugated sp^{2}c-HPTP-Ph-COF (Supplementary Figs. 47−49) as photocatalysts under otherwise identical conditions. Surprisingly, the hexagonal non-conjugated TFPB-Ph-COF exhibited a H_2O_2 production rate of only 1.4 mmol g^{-1} h^{-1}, suggesting the importance of a trigonal topology in photocatalysis (Supplementary Fig. 40). Noticeably, partially π-conjugated Im-HPTP-Ph-COF and fully π-conjugated sp^{2}c-HPTP-Ph-COF displayed low H_2O_2 production rate of only 1.1 and 2.4 mmol g^{-1} h^{-1}, respectively
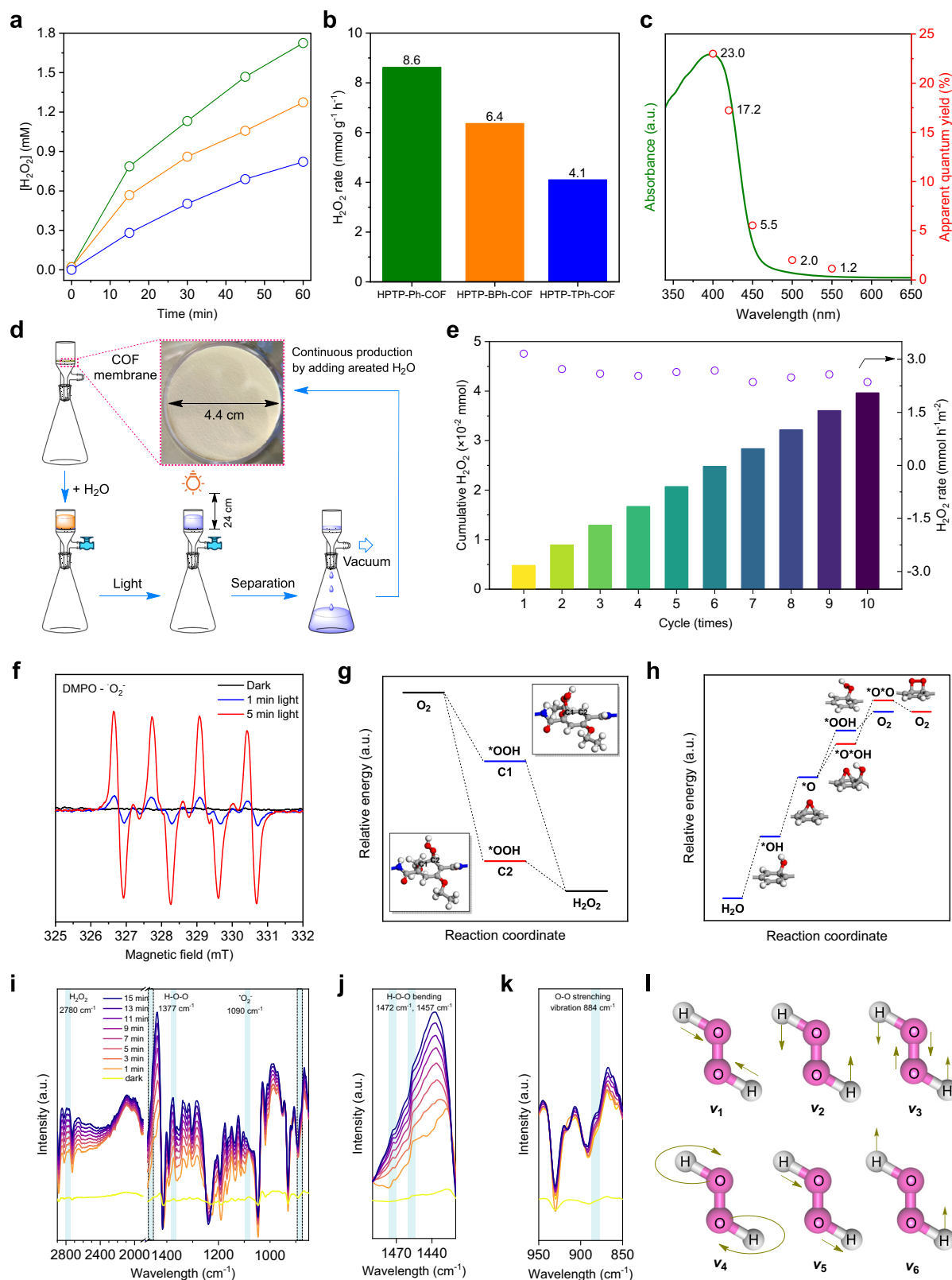
Fig. 5 | Artificial photosynthesis and photocatalytic processes. a Photocatalytic H_2O_2 production under 60-min visible light irradiation ($\lambda = 420–600$ nm) in batch reactors. **b** H_2O_2 production rate. **c** Apparent quantum yield (red circle) and electronic absorption spectrum (green curve) of HPTP-Ph-COF. **d** Membrane reactors of HPTP-Ph-COF for continuous H_2O_2 manufacture. Inset: HPTP-Ph-COF membrane. **e** Photocatalytic H_2O_2 production with membrane reactors. **f** Electron paramagnetic resonance (EPR) spectra of HPTP-Ph-COF. **g** Gibbs free energy diagram for oxygen reduction reaction over the Ph linker of HPTP-Ph-COF. **h** Gibbs free energy diagram for water oxidation at the phenyl site of the hexaphenyl triphenylene knot. **i–k** In situ diffuse reflectance infrared Fourier transform spectroscopy (DRIFTS) of HPTP-Ph-COF collected at different irradiation times during the photosynthesis under O_2 (**i**), enlarged region of 1437–1475 cm^{-1} (**j**) and 850–915 cm^{-1} (**k**). **l** Vibrational modes of H_2O_2.

(Supplementary Fig. 40). These results unambiguously demonstrated that non-conjugated trigonal COFs are superior to partially π-conjugated and fully π-conjugated COFs in photocatalytic H_2O_2 production (Supplementary Note 2).

Remarkably, HPTP-Ph-COF showed an apparent quantum yield of 23.0% at 400 nm (Fig. 5c) and a solar-to-chemical conversion efficiency of 1.06% (Supplementary Fig. 50). The solar-to-chemical conversion efficiency is over ten-fold higher than the typical photosynthetic efficiency of plants (~0.1%)[15]. We summarized typical types of photocatalysts, including covalent triazine frameworks, MOFs, g-C_3N_4, inorganic semiconductors, COFs and others (Supplementary Table 6). Notably, the photocatalytic performance for HPTP-Ph-COF is the highest one among these representative examples.

Surprisingly, HPTP-Ph-COF harvests natural sunlight to produce H_2O_2 under outdoor open conditions, achieving a high production rate of 4.5 mmol g^{-1} h^{-1} (Supplementary Figs. 51 and 52). Upon irradiation with a Xe lamp (300 W) without optical filter, the H_2O_2 production rate reaches 9.5 mmol g^{-1} h^{-1}. Robustly, HPTP-Ph-COF catalyses the H_2O_2 photosynthesis with different reaction media. For instance, it attains a production rate of 6.7 mmol g^{-1} h^{-1} in a 3.5 wt% NaCl solution and 6.6 mmol g^{-1} h^{-1} in natural seawater (Supplementary Fig. 53a). Adding a small content of alcohol to water greatly enhances the performance to reach a H_2O_2 production rate of 9.3 mmol g^{-1} h^{-1} in water/ethanol (9/1) and 27.7 mmol g^{-1} h^{-1} in water/benzyl alcohol (9/1), respectively (Supplementary Fig. 53a). HPTP-Ph-COF is robust for cycle use and produces H_2O_2 constantly (Supplementary Fig. 54). Notably, HPTP-Ph-COF produces H_2O_2 at a rate of 2.1 mmol g^{-1} h^{-1} at 60 °C. It works well in acidic (pH = 3) and base (pH = 10) conditions to generate H_2O_2 at a rate of 4.5 and 5.6 mmol g^{-1} h^{-1}, respectively (Supplementary Fig. 53b). These results suggest that HPTP-Ph-COF is robust to retain photocatalytic activity in harsh reaction conditions.

Photosynthesis in membrane reactors

HPTP-Ph-COF (15 mg) was dispersed in deionized water (30 mL) and filtered over 0.22-μm PTFE film in a sand core funnel to afford a membrane (Fig. 5d, see experimental details in Section 1.24). After adding air-saturated deionized water (30 mL) into the funnel, the membrane was irradiated with visible light (λ = 420–600 nm) to facilitate the photocatalytic reaction (Fig. 5d). Remarkably, we found that the membrane reactor steadily produces H_2O_2 solution, showing a high and constant H_2O_2 production rate of 2.61 mmol h^{-1} m^{-2} (Fig. 5e). A total 300-mL H_2O_2 solution with a concentration of 0.13 mM was produced with the membrane reactor after 10 cycles (Fig. 5e).

FT IR spectra of the recycled HPTP-Ph-COF revealed clear characteristic vibration bands of the hydrazone linkage (Supplementary Fig. 55). A slight reduction in the PXRD peak intensity (Supplementary Fig. 56) and surface area (Supplementary Figs. 57) might originate from the exfoliation of layer structures during photocatalysis, as reported previously[42,43]. We excluded the possibility of metal contamination in the photocatalytic system, as revealed by inductively coupled plasma mass spectrometry (Supplementary Table 7). These results suggest that HPTP-Ph-COF is a high-performance photocatalyst for continuous and efficient photosynthesis using water and air to produce H_2O_2.

Photocatalytic centres and reaction intermediates

Photosynthesis with water and air to produce H_2O_2 involves two half-reactions of oxygen reduction and water oxidation. To reveal the photocatalytic sites and reaction intermediates, we conducted a series of control experiments and performed computational studies (Fig. 5f–l). For the oxygen reduction half-reaction, the following experiments were carried out to identify the reaction intermediates and catalytic sites: (1) No H_2O_2 was detected in the dark, suggesting the

reaction was driven by light (Supplementary Fig. 58). (2) No H_2O_2 was generated when replacing air with argon; while using the oxygen-saturated water increases the H_2O_2 production rate to 9.0 mmol g^{-1} h^{-1}, demonstrating that O_2 is indeed involved (Supplementary Fig. 58). (3) To investigate the oxygen reduction pathway, we conducted electron paramagnetic resonance (EPR) measurement by using 5,5-dimethyl-1-pyrroline N-oxide (DMPO) as a spin trap, which reacts with superoxide radical anion ($^•O_2^-$) to form DMPO-$^•O_2^-$ adduct. The characteristic peaks of DMPO-$^•O_2^-$ adduct and increased peak intensity with the irradiation time (Fig. 5f) revealed the involvement of $^•O_2^-$ and verified a two-step oxygen reduction mechanism (Fig. 3c, dashed pink line, −0.35 V). (4) We calculated the free energy of O_2 adsorption on the skeleton and found that the linker unit of three COFs offers the most favourable site (Supplementary Figs. 59–61), where HPTP-Ph-COF exhibited the optimal adsorption energy among the series due to the formation of hydrogen bond between O_2 and the H−N unit of the hydrazone linkage (Supplementary Fig. 61). This hydrogen-bonding interaction stabilizes the O_2 adsorption on HPTP-Ph-COF, while HPTP-BPh-COF and HPTP-TPh-COF do not trigger hydrogen-bonding interactions with O_2 (Supplementary Fig. 59). (5) The oxygen reduction centre is identified to be the C1 site at the phenyl linker based on the Gibbs free energy calculations, which offers the lowest overpotential for the *OOH intermediate (Fig. 5g).

The in situ diffuse reflectance infrared Fourier transform spectroscopy (DRIFTS) measurements revealed the characteristic peak at 1084 cm^{-1} assigned to the vibration of $^•O_2^-$ intermediate (Fig. 5i–k). Notably, we observed the prominent growth of peaks from H_2O_2, including O−H vibration (Fig. 5i, l, combination of $v_2 + v_3 + v_4$: 2780 cm^{-1}), H−O−O bending vibration (Figs. 5j and 5l, $v_2 + v_6$: 1385 cm^{-1}, 1460 cm^{-1}, and 1470 cm^{-1}) and O−O stretching vibration (Fig. 5k, l, v_3: 886 cm^{-1})[44–46]. These peaks increase their intensities greatly with the irradiation time, indicating a progressed production of H_2O_2.

We investigated the water oxidation half-reaction by conducting the following systematic control experiments as well as computational calculations. (1) Adding tert-butanol as a hydroxyl radical ($^•OH$) scavenger to the reaction system does not change the H_2O_2 production rate, indicating that $^•OH$ is not involved (Supplementary Fig. 58). This is supported by the fact that COFs do not possess an energy potential high enough to enable water oxidation via $^•OH$-involved pathway (Fig. 3c, grey dashed line, +2.33 V). (2) Adding electron scavenger $NaIO_3$ to the reaction system quenches H_2O_2 generation (Supplementary Fig. 58), excluding the possibility of one-step water oxidation pathway (Fig. 3c, dashed grey line, +1.36 V). (3) Computational studies reveal a plausible catalytic site at the phenyl units of the triphenylene knot (Fig. 5h), where water oxidation occurs via a four-electron-involved process (Fig. 3c, dashed red line, +0.83 V). (4) Isotopic labelling experiments with $H_2^{18}O$ confirmed the evolution of $^{18}O_2$ (Supplementary Fig. 62), verifying that water oxidation involves in the photocatalytic cycle.

Photoexcitation of HPTP-Ph-COF generates electrons and holes, which are spatially separated on the linker and knot π units and accumulated in the columnar knot and linker π arrays, respectively, while the supermicropores deliver water and oxygen timely to the catalytic sites (Supplementary Fig. 63). The Ph linker arrays with accumulated electrons (Supplementary Fig. 63a, b) catalyse oxygen reduction ($O_2 + 2H^+ + 2e^- \rightarrow H_2O_2$), while the HPTP knot columns with collected holes (Supplementary Fig. 63c, d) facilitate water oxidation ($2H_2O \rightarrow O_2 + 4H^+ + 4e^-$), thereby completing the photosynthetic cycle ($2H_2O + O_2 \rightarrow 2H_2O_2$).

Discussion

As the photoredox process generates reactive oxygen species, we try to use the photocatalyst to decompose Rhodamine B (RhB), which is widely used in and released from the textile, leather, coloured glass,
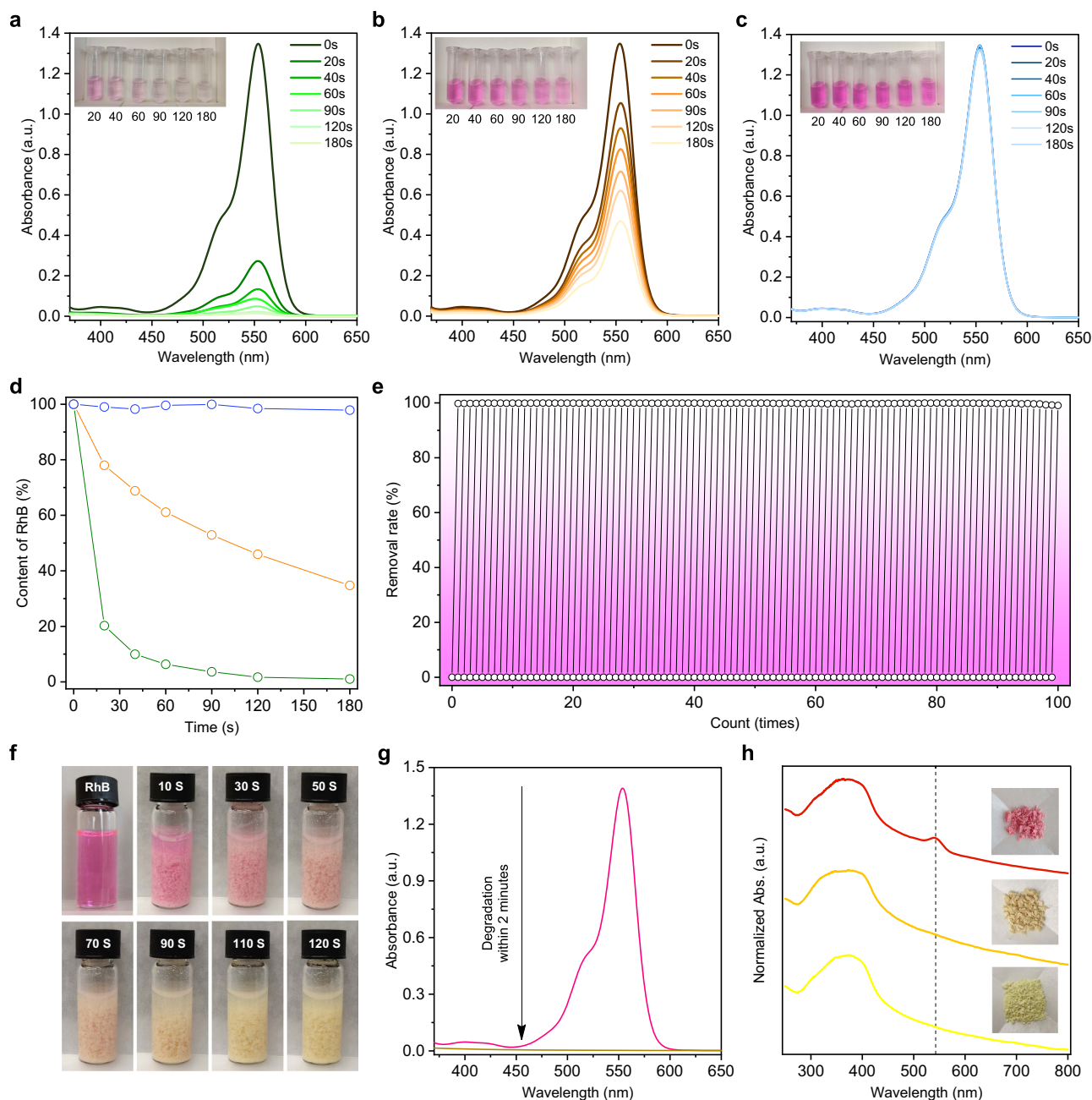
Fig. 6 | Adsorption and in-situ degradation of organic dyes. a–c Adsorption of RhB by HPTP-Ph-COF (**a**), activated charcoal (**b**) and molecular sieve (**c**). Insets are the digital photos of RhB solution sampling at different duration in second after adding absorbents. **d** RhB adsorption rate by HPTP-Ph-COF (green curve), activated charcoal (orange curve) and molecular sieve (blue curve). **e** Repetitive use of HPTP-Ph-COF in the adsorption of RhB. **f** Digital photos of RhB solution after irradiation for different durations. **g** Solution-state electronic absorption spectra of RhB before adding HPTP-Ph-COF (magenta curve) and after 2-min photo irradiation at $\lambda = 420–600$ nm (brown curve). **h** Solution-state electronic absorption spectra and digital photos (insets) of pristine HPTP-Ph-COF (yellow curve), HPTP-Ph-COF adsorbed with RhB (magenta curve) and HPTP-Ph-COF adsorbed with RhB after photodegradation (orange curve).

paper printing, paint and plastic industries to environment and is suspected to be carcinogenic. Initially, we dispersed HPTP-Ph-COF (10 mg) in aqueous solution of RhB (2 mL, 0.03 mM) and bubbled the solution by compressed air in the dark, while we observed a significant colour fading after bubbling for 5 min. This may be attributed to the adsorption of RhB by COFs[47,48]. To test our hypothesis, we performed an adsorption experiment (see detailed procedures in Supplementary Information Section 1.30) and found that the RhB molecules were instantly adsorbed after adding HPTP-Ph-COF (Supplementary Video 1) and were fully removed from solution within 1 min (Supplementary Fig. 64). These results suggested that HPTP-

Ph-COF has exceptional adsorption capability for removing dyes from aqueous media.

To further evaluate the adsorption capability of HPTP-Ph-COF, we chose commercially available activated charcoal and molecular sieve powder as reference samples (Fig. 6a–d). Surprisingly, HPTP-Ph-COF (Fig. 6a) and activated charcoal (Fig. 6b) can uptake RhB from aqueous solutions, while molecular sieve (Fig. 6c) hardly adsorbs RhB. Noticeably, HPTP-Ph-COF (Fig. 6d, green curve, Supplementary Fig. 65a and Supplementary Table 8) exhibited a high adsorption rate of 1.76 mM RhB per gramme of adsorbent per second, which is over ten-time higher than that of activated charcoal (0.14 mM RhB per gramme of

adsorbent per second, Fig. 6d, orange curve, Supplementary Fig. 65b and Supplementary Table 8). We then examined the stability of COF adsorbent via repetitive use (Fig. 6e and Supplementary Figs. 66 and 67) and found that HPTP-Ph-COF performed steadily over 100 times, while retaining high removal rate over 99% (Fig. 6e).

Remarkably, HPTP-Ph-COF enables in-situ rapid decomposition of the absorbed RhB under visible light (λ = 420–600 nm) and exhibits a near 100% degradation within 2 min (Fig. 6f–h). The decomposition of RhB can be attributed to the oxidation of the central carbon of RhB followed by the degradation via the N-de-ethylation process[49–51].

The exceptional adsorption capability and photodegrading efficiency of HPTP-Ph-COF are attributed to its supermicropores and highly photoactive skeletons, which promote mass delivery across the 1D channels and charge supply to the catalytic sites to efficiently produce reactive oxygen species.

Through the systematic and comparative studies, this work discloses the rational design of frameworks for efficient photosynthesis using water and air to produce H_2O_2. Firstly, the hexavalent connectivity is a prerequisite, which endows the frameworks not only with the highest π density but also with the smallest pores—the two factors that controls the charge in π columns and mass transport across pores. Secondarily, non-conjugated linkages such as hydrazone is essential, which allows the π skeleton to be electronically segregated so that the HOMO and LUMO are localized at the knot and linker sites, which upon photoirradiation convert into oxidation and reduction centres with optimal redox potentials, respectively. Thirdly, the skeleton needs to be photoconductive and catalytically active to generate, transport and harness charges for photosynthesis, with built-in mechanism to prevent charge recombination. Fourthly, the pores are required to be able to deliver water and dissolved oxygen timely and rapidly to the catalytic sites, enabling the efficient utilization of charges and reactants for photo-to-chemical transformation. Finally, a synergy of these structures is necessary to achieve efficient photosynthesis; lacking one aspect greatly reduces the efficiency and activity. Explicitly, the framework photocatalysts instantly trap organic dyes from water within their supermicropores and fully and rapidly degrade these dyes upon visible light irradiation. These findings offer a general guidance for developing advanced photocatalytic porous framework materials, while the green photo-to-chemical conversions offers key processes in developing sustainable society and future.

Methods
HPTP-Ph-COF
A 1,2-dichlorobenzene/propionitrile (o-DCB/PCN = 0.5 mL/0.5 mL) mixture of 2,3,6,7,10,11-hexakis(4-formylphenyl) triphenylene (17.1 mg 0.02 mmol) and 2,5-diethoxyterephthalohydrazide (16.9 mg, 0.06 mmol) in a Pyrex tube (10 mL) was sonicated for 5 min and followed by addition of acetic acid (0.5 mL, 12 M). After degassed via three freeze-pump-thaw cycles, the tube was sealed and heated at 150 °C for 3 days. The precipitate was collected by suction filtration, washed with THF three times (15 mL × 3) and Soxhlet extracted with THF overnight. The powder was dried at 120 °C under vacuum to afford HPTP-Ph-COF in an isolated yield of 91%. Elemental analysis: Calculated: C, 80.80%; H, 5.07%; N, 6.59%. Found C, 69.81%; H, 4.56%; N, 8.56%. For synthetic procedures of other COFs and controls, see Supplementary Information Section 2.2.

Data availability
Experimental data are provided with this paper and in the supplementary materials. Any additional data that support the findings of this study are available from the corresponding authors upon request. Source data are provided with this paper.

References
1. Nilsson, A. & Pettersson, L. G. M. The structural origin of anomalous properties of liquid water. *Nat. Commun.* **6**, 8998 (2015).
2. Tan, K. T., Tao, S., Huang, N. & Jiang, D. Water cluster in hydrophobic crystalline porous covalent organic frameworks. *Nat. Commun.* **12**, 6747 (2021).
3. Burtch, N. C., Jasuja, H. & Walton, K. S. Water stability and adsorption in metal-organic frameworks. *Chem. Rev.* **114**, 10575–10612 (2014).
4. Canivet, J., Fateeva, A., Guo, Y., Coasne, B. & Farrusseng, D. Water adsorption in MOFs: fundamentals and applications. *Chem. Soc. Rev.* **43**, 5594–5617 (2014).
5. Zhi, Y. et al. Covalent organic frameworks as metal-free heterogeneous photocatalysts for organic transformations. *J. Mater. Chem. A* **5**, 22933–22938 (2017).
6. Tao, S. & Jiang, D. Covalent organic frameworks for energy conversions: current status, challenges, and perspectives. *CCS Chem.* **3**, 2003–2024 (2021).
7. Gust, D., Moore, T. A. & Moore, A. L. Solar fuels via artificial photosynthesis. *Acc. Chem. Res.* **42**, 1890–1898 (2009).
8. Zhang, T. & Lin, W. Metal–organic frameworks for artificial photosynthesis and photocatalysis. *Chem. Soc. Rev.* **43**, 5982–5993 (2014).
9. Gong, Y.-N., Guan, X. & Jiang, H.-L. Covalent organic frameworks for photocatalysis: Synthesis, structural features, fundamentals and performance. *Coord. Chem. Rev.* **475**, 214889 (2023).
10. Tachibana, Y., Vayssieres, L. & Durrant, J. R. Artificial photosynthesis for solar water-splitting. *Nat. Photonics* **6**, 511–518 (2012).
11. Liu, R. et al. Linkage-engineered donor–acceptor covalent organic frameworks for optimal photosynthesis of hydrogen peroxide from water and air. *Nat. Catal.* **7**, 195–206 (2024).
12. Chen, Y. et al. Hierarchical assembly of donor–acceptor covalent organic frameworks for photosynthesis of hydrogen peroxide from water and air. *Nat. Synth.* **3**, 998–1010 (2024).
13. Chen, Y. & Jiang, D. Molecular design of covalent organic framework photocatalysts. *Nat. Synth.* **3**, 939–940 (2024).
14. Chang, J.-N. et al. Oxidation-reduction molecular junction covalent organic frameworks for full reaction photosynthesis of H_2O_2. *Angew. Chem. Int. Ed.* **62**, e202218868 (2023).
15. Chen, Y. & Jiang, D. Photocatalysis with covalent organic frameworks. *Acc. Chem. Res.* **57**, 3182–3193 (2024).
16. Mase, K., Yoneda, M., Yamada, Y. & Fukuzumi, S. Seawater usable for production and consumption of hydrogen peroxide as a solar fuel. *Nat. Commun.* **7**, 11470 (2016).
17. Yong, Z. & Ma, T. Solar-to-H_2O_2 catalyzed by covalent organic frameworks. *Angew. Chem., Inter. Ed.* **62**, e202308980 (2023).
18. Sun, J. et al. Metal–organic frameworks and covalent organic frameworks as photocatalysts for H_2O_2 production from oxygen and water. *J. Mater. Chem. A* **11**, 21516–21540 (2023).
19. Wang, H., Yang, C., Chen, F., Zheng, G. & Han, Q. A crystalline partially fluorinated triazine covalent organic framework for efficient photosynthesis of hydrogen peroxide. *Angew. Chem., Int. Ed.* **61**, e202202328 (2022).
20. Zhai, L. et al. Constructing synergistic triazine and acetylene cores in fully conjugated covalent organic frameworks for cascade photocatalytic H_2O_2 production. *Chem. Mater.* **34**, 5232–5240 (2022).
21. Yang, Y. et al. Enhanced photocatalytic hydrogen peroxide production activity of imine-linked covalent organic frameworks via modification with functional groups. *N. J. Chem.* **46**, 21605–21614 (2022).
22. Hu, H. et al. Rational modification of hydroxy-functionalized covalent organic frameworks for enhanced photocatalytic hydrogen peroxide evolution. *J. Colloid Interf. Sci.* **629**, 750–762 (2023).

23. Wu, M., Shan, Z., Wang, J., Liu, T. & Zhang, G. Three-dimensional covalent organic framework with tty topology for enhanced photocatalytic hydrogen peroxide production. *Chem. Eng. J.* **454**, 140121 (2023).

24. He, T. & Zhao, Y. Covalent organic frameworks for energy conversion in photocatalysis. *Angew. Chem. Int. Ed.* **62**, e202303086 (2023).

25. Li, G. et al. Boosting exciton dissociation by regulating dielectric constant in covalent organic framework for photocatalysis. *Chem. Catal.* **2**, 1734–1747 (2022).

26. Geng, K. et al. Covalent organic frameworks: design, synthesis, and functions. *Chem. Rev.* **120**, 8814–8933 (2020).

27. Jin, E. et al. 2D sp^2 Carbon-conjugated covalent organic frameworks for photocatalytic hydrogen production from water. *Chemistry* **5**, 1632–1647 (2019).

28. Munoz-Santiburcio, D. & Marx, D. Nanoconfinement in slit pores enhances water self-dissociation. *Phys. Rev. Lett.* **119**, 056002 (2017).

29. Musat, R. et al. Finite size effects on hydrogen bonds in confined water. *Angew. Chem. Int. Ed.* **47**, 8033–8035 (2008).

30. Goettmann, F. & Sanchez, C. How does confinement affect the catalytic activity of mesoporous materials?. *J. Mater. Chem.* **17**, 24–30 (2007).

31. Thomas, A., Polarz, S. & Antonietti, M. Influence of spatial restrictions on equilibrium reactions: a case study about the excimer formation of pyrene. *J. Phys. Chem. B* **107**, 5081–5087 (2003).

32. Stolte, N., Hou, R. & Pan, D. Nanoconfinement facilitates reactions of carbon dioxide in supercritical water. *Nat. Commun.* **13**, 5932 (2022).

33. Grommet, A. B., Feller, M. & Klajn, R. Chemical reactivity under nanoconfinement. *Nat. Nanotechnol.* **15**, 256–271 (2020).

34. Segura, J. L., Mancheño, M. J. & Zamora, F. Covalent organic frameworks based on Schiff-base chemistry: synthesis, properties and potential applications. *Chem. Soc. Rev.* **45**, 5635–5671 (2016).

35. Smirnova, O. et al. Tiny windows in reticular nanomaterials for molecular sieving gas separation membranes. *Adv. Funct. Mater.* **34**, 2306202 (2024).

36. Knebel, A. A. & Caro, J. Metal–organic frameworks and covalent organic frameworks as disruptive membrane materials for energy-efficient gas separation. *Nat. Nanotechnol.* **17**, 911–923 (2022).

37. Shaegh, S. A. M., Nguyen, N.-T., Ehteshami, S. M. M. & Chan, S. H. A membraneless hydrogen peroxide fuel cell using Prussian blue as cathode material. *Energ. Environ. Sci.* **5**, 8225–8228 (2012).

38. Krishnaraj, C. et al. Strongly reducing (diarylamino)benzene-based covalent organic framework for metal-free visible light photocatalytic H$_2$O$_2$ generation. *J. Am. Chem. Soc.* **142**, 20107–20116 (2020).

39. Kou, M. P. et al. Molecularly engineered covalent organic frameworks for hydrogen peroxide photosynthesis. *Angew. Chem., Int. Ed.* **61**, e202200413 (2022).

40. Zhi, Q. et al. Piperazine-linked metalphthalocyanine frameworks for highly efficient visible-light-driven H$_2$O$_2$ photosynthesis. *J. Am. Chem. Soc.* **144**, 21328–21336 (2022).

41. Tan, F. et al. Aqueous synthesis of covalent organic frameworks as photocatalysts for hydrogen peroxide production. *CCS Chem.* **4**, 3751–3761 (2022).

42. Bunck, D. N. & Dichtel, W. R. Bulk Synthesis of Exfoliated Two-dimensional polymers using hydrazone-linked covalent organic frameworks. *J. Am. Chem. Soc.* **135**, 14952–14955 (2013).

43. Stegbauer, L., Schwinghammer, K. & Lotsch, B. V. A hydrazone-based covalent organic framework for photocatalytic hydrogen production. *Chem. Sci.* **5**, 2789–2793 (2014).

44. Voraberger, H., Ribitsch, V., Janotta, M. & Mizaikoff, B. Application of mid-infrared spectroscopy: measuring hydrogen peroxide concentrations in bleaching baths. *Appl. Spectrosc.* **57**, 574–579 (2003).

45. Giguère, P. A. The infra-red spectrum of hydrogen peroxide. *J. Chem. Phys.* **18**, 88–92 (1950).

46. Żegliński, J., Piotrowski, G. P. & Piękos´, R. A study of interaction between hydrogen peroxide and silica gel by FTIR spectroscopy and quantum chemistry. *J. Mol. Struct.* **794**, 83–91 (2006).

47. Fan, H., Gu, J., Meng, H., Knebel, A. & Caro, J. High-flux membranes based on the covalent organic framework COF-LZU1 for selective dye separation by nanofiltration. *Angew. Chem., Int. Ed.* **57**, 4083–4087 (2018).

48. Wang, P. et al. High-precision size recognition and separation in synthetic 1D nanochannels. *Angew. Chem., Int. Ed.* **58**, 15922–15927 (2019).

49. Sharma, G. et al. Highly efficient Sr/Ce/activated carbon bimetallic nanocomposite for photoinduced degradation of Rhodamine B. *Catal. Today* **335**, 437–451 (2019).

50. He, Y., Zhou, S., Wang, Y., Jiang, G. & Jiao, F. Fabrication of g-C3N4@NiFe-LDH heterostructured nanocomposites for highly efficient photocatalytic removal of Rhodamine B. *J. Mater. Sci.* **32**, 21880–21896 (2021).

51. Abouri, M. et al. Enhanced photocatalytic degradation of Rhodamine B using polyaniline-coated XTiO$_3$(X = Co, Ni) nanocomposites. *Sci. Rep.* **15**, 3595 (2025).

Acknowledgements

Author contributions

D.J. conceived the idea and led the project. Y.C. conducted the experiments and calculations. Y.G. conducted the transient absorption measurements. T.W. and N.Y. conducted the DRIFTS and XPS measurements. S.J. and S.S. conducted the transient photoconductivity measurements. H.S. and M.L. conducted the transmission electron microscopy. Y.C., Y.G., T.W., S.J., H.S., M.L., N.Y., S.S. and D.J. interpreted the results and Y.C. and D.J. wrote the paper. All authors have read and commented on the paper.

Competing interests

The authors declare no competing interests.

Additional information

Supplementary information The online version contains supplementary material available at https://doi.org/10.1038/s41467-025-61853-4.

Correspondence and requests for materials should be addressed to Donglin Jiang.

Peer review information *Nature Communications* thanks Pascal Van Der Voort and the other, anonymous, reviewers for their contribution to the peer review of this work. A peer review file is available.

Reprints and permissions information is available at http://www.nature.com/reprints

Publisher's note Springer Nature remains neutral with regard to jurisdictional claims in published maps and institutional affiliations.